Identification of a series of pyrrolo-pyrimidine based SARS-CoV-2 Mac1 inhibitors that repress coronavirus replication

Jessica J. Pfannenstiel[1], Men Thi Hoai Duong[2], Daniel Cluff[1], Lavania M. Sherrill[3], Iain Colquhoun[3], Gabrielle Cadoux[3], Devyn Thorne[3], Johan Pääkkönen[2], Nathaniel F. Schemmel[1], Joseph O'Connor[1], Pradtahna Saenjamsai[1], Mei Feng[4], Michael J. Hageman[4,5], David K. Johnson[6], Anuradha Roy[7], Lari Lehtiö[2#], Dana V. Ferraris[3#], Anthony R. Fehr[1#]

[1]*Department of Molecular Biosciences, University of Kansas, Lawrence, Kansas, USA*
[2]*Faculty of Biochemistry and Molecular Medicine & Biocenter Oulu, University of Oulu, Oulu, Finland*
[3]*McDaniel College Department of Chemistry, 2 College Hill, McDaniel College, Westminster, Maryland 21157, USA*
[4]*Biopharmaceutical Innovation & Optimization Center, University of Kansas, Lawrence, Kansas 66047, USA*
[5]*Department of Pharmaceutical Chemistry, University of Kansas, Lawrence, Kansas 66047, USA*
[6]*Molecular Graphics and Modeling Laboratory and the Computational Chemical Biology Core, University of Kansas, Lawrence, Kansas, USA*
[7]*Infectious Disease Assay Development Laboratory/HTS, University of Kansas, Lawrence, Kansas, USA*

[#]Corresponding authors:
Email addresses: lari.lehtio@oulu.fi (L. Lehtiö), dferraris@mcdaniel.edu (D. Ferraris), arfehr@ku.edu (A.R. Fehr).

Keywords: SARS-CoV2, COVID-19, coronavirus, Murine Hepatitis Virus, COVID-19, nsp3 macrodomain, ADP-ribosylation

ABSTRACT

Coronaviruses (CoVs) can emerge from zoonotic sources and cause severe diseases in humans and animals. All CoVs encode for a macrodomain (Mac1) that binds to and removes ADP-ribose from target proteins. SARS-CoV-2 Mac1 promotes virus replication in the presence of interferon (IFN) and blocks the production of IFN, though the mechanisms by which it mediates these functions remain unknown. Mac1 inhibitors could help elucidate these mechanisms and serve as therapeutic agents against CoV-induced diseases. We previously identified compound **4a** (a.k.a. MCD-628), a pyrrolo-pyrimidine that inhibited Mac1 activity *in vitro* at low micromolar levels. Here, we determined the binding mode of **4a** by crystallography, further defining its interaction with Mac1. However, **4a** did not reduce CoV replication, which we hypothesized was due to its acidic side chain limiting permeability. To test this hypothesis, we developed several hydrophobic derivatives of **4a**. We identified four compounds that both inhibited Mac1 *in vitro* and inhibited murine hepatitis virus (MHV) replication: **5a**, **5c**, **6d**, and **6e**. Furthermore, **5c** and **6e** inhibited SARS-CoV-2 replication only in the presence of IFNγ, similar to a Mac1 deletion virus. To confirm their specificity, we passaged MHV in the presence of **5a** to identify drug-resistant mutations and identified an alanine-to-threonine and glycine-to-valine double mutation in Mac1. Recombinant virus with these mutations had enhanced replication compared to WT virus when treated with **5a**, demonstrating the specificity of these compounds during infection. However, this virus is highly attenuated *in vivo*, indicating that drug-resistance emerged at the expense of viral fitness.

IMPORTANCE

Coronaviruses (CoVs) present significant threats to human and animal health, as evidenced by recent outbreaks of MERS-CoV and SARS-CoV-2. All CoVs encode for a highly conserved macrodomain protein (Mac1) that binds to and removes ADP-ribose from proteins, which promotes virus replication and blocks IFN production, though the exact mechanisms remain unclear. Inhibiting Mac1 could provide valuable insights into these mechanisms and offer new therapeutic avenues for CoV-induced diseases. We have identified several unique pyrrolo-pyrimidine-based compounds as Mac1 inhibitors. Notably, at least two of these compounds inhibited both murine hepatitis virus (MHV) and SARS-CoV-2 replication. Furthermore, we identified a drug-resistant mutation in Mac1, confirming target specificity during infection. However, this mutant is highly attenuated in mice, indicating that drug-resistance appears to come at a fitness cost. These results emphasize the potential of Mac1 as a drug target and the promise of structure-based inhibitor design in combating coronavirus infections.

INTRODUCTION

Coronaviruses (CoVs) are large, positive-sense RNA viruses that infect a wide variety of mammalian species, including humans. Some human CoVs (HCoVs), such as HCoV-OC43, HKU1, NL63, and HCoV-229E are endemic and contribute to the common cold, while others, severe acute respiratory syndrome (SARS)-CoV, Middle East respiratory syndrome (MERS)-CoV, and SARS-CoV-2 have caused epidemic outbreaks of severe disease and human fatalities. The recent COVID-19 pandemic caused by SARS-CoV-2 resulted in the deaths of over seven million people worldwide and had profound social and economic consequences. Beyond the devastating human toll, the pandemic disrupted healthcare systems, led to widespread economic downturns, and prompted significant changes in global public health infrastructure and policy (1). SARS-CoV-2 is now endemic in the human population and continues to cause severe disease in humans. Furthermore, many other CoVs have been identified in wildlife, posing a continuous threat of zoonotic transmission that could lead to additional epidemics (2). Thus, there is an urgent need for novel therapeutic interventions and further vaccine development.

Coronaviruses (CoVs) evade the host's innate immune response by encoding for multiple proteins that either repress the production of interferon (IFN) or directly inhibit IFN-stimulated genes (ISGs) (3, 4). Several PARP proteins are highly induced by IFN and are part of the antiviral response (5, 6). Most PARPs act as ADP-ribosyltransferases (ARTs) that add single (mono) or multiple (poly) units of ADP-ribose onto proteins (7). ADP-ribosylation can be reversed by several different classes of enzymes, including macrodomains (8). All CoVs, alphaviruses, Hepatitis E virus, and Rubella virus encode a macrodomain in their genome, indicating that a broad spectrum of positive-sense RNA viruses utilize macrodomains to reverse ADP-ribosylation during infection (9, 10). For CoVs, the conserved macrodomain is encoded within non-structural protein 3 (nsp3),

and is called Mac1. Mac1 binds to and removes ADP-ribose from protein, countering host PARPs (6, 11). Prior research has shown that murine hepatitis virus (MHV), SARS-CoV, MERS-CoV, and SARS-CoV-2 viruses engineered with point mutations that reduce Mac1 ADP-ribose binding or hydrolysis activity replicate poorly, lead to enhanced IFN and pro-inflammatory cytokine responses and cause minimal disease in animal models of infection (12-20). Furthermore, recombinant alphaviruses with macrodomain mutations are also highly attenuated in cell culture and in mice (21-23). Understanding the role of viral macrodomains in immune evasion and viral replication is crucial for developing effective therapeutic interventions and vaccines.

Interestingly, the complete deletion of SARS-CoV-2 Mac1 does not substantially impair viral replication in cell culture, which contrasts with other CoVs, such as MHV and MERS-CoV, where Mac1 deletion leads to unrecoverable viruses (18). However, SARS-CoV-2 Mac1-deletion and point mutant viruses exhibited increased sensitivity to IFN-γ, led to increased production of IFN and ISGs, and did not cause severe disease in mice (18-20). This indicates that SARS-CoV-2 Mac1 plays a critical role during infection, though its specific targets during infection and downstream consequences, such as its effect on the viral lifecycle, remain largely unknown. Mac1 inhibitors could thus be useful tools to help identify these targets and better understand how Mac1 directly promotes virus replication and pathogenesis. Furthermore, as Mac1 is completely conserved across all CoVs and is vital for viral pathogenesis, it could be a unique therapeutic target for SARS-CoV-2 and other potential pandemic CoVs (2).

Since the outbreak of SARS-CoV in 2003 and up to the start of the COVID-19 pandemic, several studies have determined the structure of Mac1 from multiple CoVs and alphaviruses, including SARS-CoV, 229E, Infectious Bronchitis Virus (IBV), MERS-CoV, HKU4, Chikungunya virus (CHIKV) and Venezuelan Equine Encephalitis virus (VEEV) (24-29). Much like

105 macrodomains that had been discovered from species such as archaea (30), the viral macrodomains
106 form an $\alpha\beta\alpha$ sandwich like structure with several β-sheets surrounded by α-helices on both sides,
107 with a highly defined ADP-ribose binding pocket. Shortly after the pandemic began, several
108 SARS-CoV-2 Mac1 structures were determined, which provided detailed atomic-level resolution
109 of the SARS-CoV-2 Mac1 protein facilitating drug-discovery efforts (11, 31-34).

110 Multiple groups have now identified Mac1 inhibitors through high-throughput screening
111 and targeted drug development using these crystal structures (35-44). Through these efforts,
112 several compounds with IC_{50} values between 0.4 and 10 μM have been discovered with high
113 specificity *in vitro* (45). One of these studies utilized a unique crystallography-based fragment
114 screen that identified several small molecules that bound to the ADP-ribose binding pocket of
115 Mac1 (35). These fragments served as promising starting points for further inhibitor development
116 for multiple groups (36, 37, 39). Starting with a small pyrrolo-pyrimidine fragment with weak *in*
117 *vitro* potency (IC_{50} of 180 μM), we synthesized a series of primary and secondary amino acid-
118 based pyrrolo-pyrimidines to determine whether more potent Mac1 inhibitors could be developed.
119 The previously described luminescent-based AlphaScreen™ (AS) assay was utilized to screen ~60
120 pyrrolo-pyrimidines for their ability to inhibit Mac1-ADP-ribose binding. Of these pyrrolo
121 pyrimidines, we identified a tryptophanate (MCD-628) that inhibited SARS-CoV-2 Mac1-ADP-
122 ribose binding with an IC_{50} of 6.1 μM. MCD-628 incubation with Mac1 also increased its thermal
123 stability to nearly the same degree as ADP-ribose, indicating that it directly binds to Mac1.
124 However, this compound contains a carboxylic acid group that suggests it would have poor
125 permeability and be unlikely to inhibit virus replication. Many potent Mac1 inhibitors have acidic
126 or highly polar moieties, likely limiting their ability to inhibit virus replication or pathogenesis
127 (45). To date, only one Mac1 inhibitor has been published that represses CoV replication in cell

culture (40). Thus, future Mac1 inhibitors must be designed to increase their inhibition of Mac1 biochemical functions *in vitro* and repress CoV replication in cell culture or animal model infections.

In this study, we solved a co-crystal structure of Mac1 with MCD-628 (termed **4a** herein) and designed a novel series of pyrrolo-pyrimidine-based Mac1 inhibitors with increased lipophilicity to identify compounds that could both inhibit Mac1 *in vitro* and repress CoV replication in cell culture. We replaced the acidic moiety of our lead compound, MCD-628 (termed **4a** herein), with several esters and amide couplings with hydrophobic pyridines. These modifications largely improved cell permeability while maintaining inhibitory activity *in vitro*. We identified four compounds that substantially repressed MHV replication in cell culture, including two that inhibited MHV and SARS-CoV-2. Importantly, these compounds only inhibited SARS-CoV-2 in the presence of IFN-γ, in-line with results demonstrating that Mac1-deleted or mutated SARS-CoV-2 viruses are highly sensitive to IFN-γ (18-20). Additionally, mutations conferring resistance to one of these inhibitors were identified, further confirming their target specificity. These findings demonstrate that Mac1 inhibitors can repress virus replication and offer a promising platform for developing Mac1 chemical probes and CoV antivirals.

RESULTS

Structural and biochemical analysis of pyrrolo-pyrimidine based SARS-CoV-2 Mac1 inhibitor. Using a series of amino acid based 7H-pyrrolo[2,3-d] pyrimidines, we previously created compound **4a** (*S*), derived from tryptophan, that inhibited SARS-CoV-2 Mac1 binding to ADP-ribose with a 6.1 μM IC_{50} value (Fig. 1A-B) (39). **4a** also inhibited Mac1 enzyme activity and bound to Mac1 as demonstrated by a thermal shift profile similar to Mac1's natural ligand,

ADP-ribose (39). Having established that **4a** binds and inhibits Mac1 *in vitro*, we sought to get more insight into the mechanism by which **4a** binds to Mac1 by determining the structure of **4a** with Mac1. We solved the structure of **4a** with Mac1 and refined it to 1.1 Å resolution (Fig. 1C-D, Table S1). In this structure, some of the key features are a hydrogen bond with D22 and the backbone of I23, multiple hydrogen bonds between the carboxylate with neighboring water molecules, and finally a hydrogen bond between the indole NH and L126 (Fig. 1C-D). F156, previously seen to form pi stacking interactions with ADP-ribose and inhibitors, has considerable flexibility, and while it is next to the pyrrolo-pyrimidine and contributes to hydrophobic interactions, the geometry does not allow pi-stacking interactions. This co-crystal structure provides a strong starting point for the synthesis of additional Mac1 inhibitors.

Next, we tested whether the enantiomer of **4a**, **4b** (*R*) (Fig. 2A), would also bind and inhibit SARS-CoV-2 Mac1. Indeed, **4b** interacted with Mac1 as it had a similar thermal shift profile to that of **4a** (Fig. 2B). Furthermore, **4b** inhibited Mac1 binding to an ADP-ribosylated peptide in an AlphaScreen assay with an IC_{50} of 1.66 μM with almost no inhibition of the Bn-His peptide control (Fig. 2C). We were able to reproduce the experimental binding mode of 4a by molecular modeling and subsequently demonstrated that **4b** would interact with Mac1 in a similar manner (Fig. 2D).

Compounds **4a**/**4b** have a negatively charged carboxylic acid moiety at physiological pH, which we hypothesized might preclude its ability to cross cellular membranes. To address this potential problem, we first replaced the carboxylic acid with methyl (**5a**/**5b**) and isopropyl (**5c**/**5d**) esters (Fig 3A). Unexpectantly, the esters derived from **4b**, **5b** and **5d**, did not demonstrate any significant inhibition of Mac1 in the AlphaScreen assay (data not shown), while the **4a** derivatives, **5a** and **5c**, interacted with Mac1 by the thermal shift assay (Fig. 3B) and inhibited Mac1 in the AlphaScreen assay with IC_{50} values of 14.14 μM and 3.66 μM, respectively (Fig. 3C). Based on

modeling, the additional carbon atoms on these molecules appear to protrude out of the binding pocket and have only minimal impact on the overall interaction of these compounds with Mac1 (Fig. 3D). Importantly, the addition of the esters dramatically increased the lipophilicity of these compounds, as the logD at pH 7.4 of these compounds went from -0.61 (**4a**) to 1.5 (**5a**) and 3.33 (**5c**), indicating that the ester-modified compounds are much more likely to cross cellular membranes and target Mac1 during infection.

Pyrrolo-pyrimidine based esters inhibits MHV-JHM replication. We next aimed to determine if these compounds could inhibit CoV replication. A SARS-CoV-2 Mac1-deletion virus had only a modest growth defect in Calu-3 cells of 2-3-fold, which indicates that Mac1 inhibitors may not impact SARS-CoV-2 replication in cell culture. In contrast, Mac1 is critical, if not essential, for the replication of murine hepatitis virus (MHV) strain JHM (JHMV) (17). Thus, we hypothesized that this virus may be better suited for testing Mac1 inhibitors for their ability to inhibit virus replication. To enable more efficient screening of compounds for impacts on virus replication, we replaced ORF4 of JHMV with nanoluciferase (JHMV-nluc) (Fig. S1), as the deletion of ORF4 does not affect JHMV replication or pathogenesis (46). JHMV-nluc replicated like WT virus (Fig. 4A) and importantly, produced over 10^6 light units at peak replication (Fig. 4B). Next, we tested the ability of **4a**, **4b**, **5a**, and **5c** to inhibit JHMV-nluc replication in DBT cells at concentrations ranging from 25 to 200 μM, using **GS441524** (active metabolite of remdesivir) as a control. DBT cells are an astrocytoma cell line that are susceptible to MHV. JHMV replication in DBT cells is highly dependent on Mac1 activity, as a D1329A mutant virus replicates very poorly in these cells (17). As expected, **4a** and **4b** did not affect JHMV replication, as opposed to **GS441524**, which inhibited virus replication at all concentrations. In contrast, both **5a** and **5c** inhibited JHMV replication, with **5c** being significantly more potent, having inhibited JHMV to nearly the same

level as **GS441524** at 25 μM (Fig. 4C). Importantly, none of these molecules showed substantial cytotoxicity at the concentrations tested (Fig. S2A-B).

Next, we tested whether **5a** or **5c** would impact the production of infectious virus. Indeed, we found that both **5a** and **5c** inhibited the production of infectious virus following infection of both DBT and L929 cells with JHMV (Fig. 4D-E). **5a** only inhibited virus production at 200 μM, while **5c** inhibited virus replication with as little as 25 μM and decreased replication by ~1.5 and 3 logs at 50 μM on DBT and L929 cells, respectively. To better determine the EC_{50} for **5c**, we tested its activity at concentrations from 0-50 μM on DBT, L292, and 17Cl-1 cells (Fig. 4F-G, S3A). The inhibition of virus production at these concentrations was dose-dependent and using this data we determined that the EC_{50} for **5c** on was ~10-20 μM, not substantially different from its IC_{50} of 3.66 μM (Fig. 4H-I, S3B).

Next, amide couplings were conducted with carboxylates **4a** and **4b** to create 25 additional compounds, many of which included highly hydrophobic side chains to increase the lipophilicity. Of these, 5 compounds demonstrated IC_{50} values of less than 10 μM in our initial screening and were named **6a**-**6e** (Fig. 5A and data not shown). Compounds **6a** and **6b** contain a pyridine group attached to the amide with the only difference being a chlorine atom on **6b**. **6d** *(S)* and **6e** *(R)* are enantiomers and only differ from **6a** in the position of the nitrogen on the pyridine. Finally, **6c** only has an amide group to replace the carboxylate. Only **6e** was derived from **4b**, while the rest were derived from **4a**. Following dose-response curves, we found that each of these 5 compounds had very similar IC_{50} values ranging from 4.0-8.4 μM in the AlphaScreen assay (Fig. 5B). They also had thermal shifts of 1-3°C in the DSF assay when incubated with the SARS-CoV-2 Mac1 protein, indicating a direct interaction with Mac1 (Fig. 5C). All of them had cLogD values between 1 and 3, indicating an increased lipophilicity compared to the parent compounds (**4a** LogD -0.61). Based

on our modeling data, the position of each of these molecules in the binding pocket does not change significantly. The only major difference is the position of the pyridine for each molecule (Fig. 5D). For **6a**, **6b**, and **6d**, the pyridine protrudes out from the pocket and into slightly different poses for each one. In contrast, the pyridine of **6e** extends into the oxyanion subsite, which could explain its slightly greater inhibition of Mac1-ADP-ribose binding in the AlphaScreen assay.

Inhibition of MHV-JHM replication by 6d and 6e. Similar to series **5**, we next tested if compounds in series **6** could inhibit virus replication. Using JHMV-nLuc, our initial screening found that only **6d** and **6e** inhibited light production from MHV replication in a dose-dependent manner (Fig. 6A). Furthermore, **6d** and **6e** demonstrated no substantial impact on cell viability (Fig. S4A-B). We next performed dose-response curves for **6d** and **6e** on both DBT and L929 cells at concentrations ranging from 50-200 μM and found that the compounds inhibited MHV in a dose-dependent manner on both cells, with better activity on DBT cells (Fig. 6B-C). Using these results, we determined that the EC_{50} value for **6d** and **6e** on DBT cells was 77.1 and 53.5 μM, respectively (Fig. 6D-E).

Compounds 5c and 6e inhibit SARS-CoV-2 replication. Having established antiviral activity against MHV, we next wanted to determine if our pyrrolo-pyrimidine based compounds could also inhibit SARS-CoV-2 replication. We hypothesized that our compounds would be more potent against SARS-CoV-2 as they were identified for their ability to inhibit the SARS-CoV-2 Mac1 protein, not the MHV Mac1 protein, *in vitro* (Figs. 3 & 5). Recently, we demonstrated that a full Mac1 deletion virus (SARS-CoV-2 ΔMac1) replicates normally in cell culture compared to WT virus except when cells are pre-treated with IFN-γ. In the presence of 100 U of IFN-γ ΔMac1 replicated ~10-fold worse than WT virus in Calu-3 cells. Thus, we hypothesized that our compounds would only inhibit SARS-CoV-2 if cells are pre-treated with IFN-γ. So, we pretreated

Calu-3 cells with IFN-γ and then infected cells in the presence or absence of **5c** or **6e** from 0 to 25 μM (Fig. 7). First, we confirmed that neither **5c** nor **6e** affected the viability of Calu-3 cells (Fig. S5). In the absence of IFN-γ, **6e** did not reduce infectious virus production, and **5c** only reduced viral titers ~2-fold at 25 μM. In contrast, each compound reduced infectious virus production in the presence of IFN-γ at both 12.5 and 25 μM (Fig. 7A-B). **5c** reduced viral titers by 3 and 7.5-fold, while **6e** reduced them by 2.7 and 3.8-fold at 12.5 and 25 μM, respectively, indicating that the EC_{50} for each compound would be no greater than 12.5 μM, again similar to their IC_{50} values. These results demonstrate that our pyrrolo-pyrimidine based Mac1 inhibitors are more potent against SARS-CoV-2 and the fact that they only inhibit virus production in the presence of IFN-γ strongly indicates that they specifically target Mac1 at the concentrations tested.

To further demonstrate the specificity of our compounds, we looked to identify drug-resistant mutations in JHMV. We used JHMV for these experiments to avoid any potential gain of function issues with SARS-CoV-2 virus. We passaged 3 separate biological replicates of JHMV 3X in the presence of 150 μM **5a** (5a1, 5a2, 5a3) (Fig. 8A). At this concentration **5a** inhibits infectious virus production by ~0.5 logs, so that we would get a suitable concentration of virus produced to continue passaging (Fig. 8B). Virus exposed to **5a** became resistant by passage 2. We then took passage 3 virus and plaque-picked two separate biological replicates twice before sequencing the macrodomain from each isolate. In one of the plaque picked viruses, we identified two macrodomain mutations in neighboring residues, A1438T and G1439V (Fig. 8C). Remarkably, these are the same mutations that appeared in previous work with a different compound (40). Furthermore, we had engineered a recombinant virus with these mutations in a prior study evaluating different point mutants of Mac1, which demonstrated that this virus replicated at near WT levels in cell culture but was highly attenuated in mice (17). Notably, the

A1438T/G1439V recombinant virus had increased replication compared to WT virus in the presence of **5a** (Fig. 8D). This result demonstrates that these mutations confer some resistance to **5a** and suggests that it targets Mac1. We also found that this virus had increased replication in the presence of **5c**, though the increase was not statistically significant (Fig. 8D).

In total, we developed a series of pyrrolo-pyrimidine based compounds that inhibit Mac1 activity *in vitro* and also repress both MHV and SARS-CoV-2 replication in cell culture by specifically targeting Mac1.

DISCUSSION

Coronaviruses (CoVs) remain a global health threat, as demonstrated by the SARS-CoV-2 pandemic and earlier outbreaks of SARS-CoV and MERS-CoV. Over the past two decades, research on the conserved CoV macrodomain (Mac1) has found that it is critical for pathogenesis and promotes virus replication in the presence of interferon (IFN). The development of Mac1 inhibitors offers therapeutic potential and serves as a valuable strategy for probing the underlying mechanisms by which Mac1 promotes viral pathogenesis. In this study, we focused on improving previously developed Mac1 inhibitors as both chemical and antiviral agents (39).

While reverse genetics has proven to be a powerful tool in understanding Mac1 biology, there are several limitations to CoV reverse genetic systems. First, they are not available to all researchers; deletion mutations are not always recoverable and may have undesired impacts on neighboring genes, point mutations may not fully attenuate the functions of the protein, and they do not allow for temporal evaluation of function. Developing molecular probes targeting SARS-CoV-2 Mac1 would help uncover Mac1's biological functions and advance our understanding of CoV biology, particularly how CoVs evade the host immune response. Specifically, Mac1 targeting

289 probes offer an additional method to investigate how ADP-ribosylation, a process reversed by
290 Mac1, impacts the interaction between the virus and host immune responses and disease outcomes
291 during CoV infection both *in vitro* and *in vivo*. This is exemplified by previous studies where
292 SARS-CoV-2 Mac1 deletion or mutation in animal models leads to attenuation of viral replication
293 and enhanced interferon production, suggesting that effective Mac1 inhibition could weaken the
294 virus while strengthening host defenses (18, 19).

295 Previously we expanded upon a prior fragment screen and identified several pyrrolo-
296 pyrimidine based compounds with IC_{50} values less than 25 μM. Pyrrolo-pyrimidine-based
297 compounds are promising candidates as Mac1 inhibitors due to their molecular mimicry of
298 adenine, which enables them to fit effectively into the ADP-ribose binding pocket of Mac1. This
299 mimicry facilitates strong interactions within the Mac1's active site, making these compounds
300 valuable starting points for inhibitor development (35, 39). The most potent pyrrolo-pyrimidine
301 from our previous work was **4a** (MCD-628), a tryptophanate. Furthermore, its enantiomer, **4b**, had
302 even more potent inhibitory activity against Mac1 with an IC_{50} below 2 μM. Here, we solved the
303 crystal structure of **4a** with Mac1, which revealed key interactions such as hydrogen bonds with
304 the amino acids D22 and I23, nearby water molecules and between the indole NH group and L126.

305 While **4a** inhibited Mac1 activity *in vitro*, its physicochemical properties, most notably a
306 prominent carboxylic acid that contributed to its negative logD value, were significant
307 impediments to its antiviral activity. Many of the published Mac1 inhibitors, including those we
308 synthesized, contain polar or acidic moieties that could limit their cellular permeability, which is
309 a key determinant in translating *in vitro* activity into cell culture and *in vivo* efficacy. To address
310 this problem, those moieties were initially modified to methyl and isopropyl ester groups to
311 improve the lipophilicity of the compounds, as demonstrated with derivatives **5a** and **5c**, which

had substantially improved logD values compared to **4a**. Despite the modest impact of these modifications on Mac1 inhibition, increasing the logD value correlated with their ability to inhibit virus replication. Interestingly, the **4a**, but not the **4b**-derived esters, inhibited Mac1 activity *in vitro* despite **4b** being the more potent inhibitor. Based on the co-crystal structure of **4a** and the docking model of **4b** (Fig. 2) the esterification could create some steric clash with the pyrimidine in the active conformation binding to Mac1. This was also observed in amide derivatives **6a-6e** where only **6e** derived from **4b** was active and predicted to have a distinct binding mode from the enantiomer **6d** (Fig. 6E).

To further explore the potential for replacing the carboxylate of **4a**/**4b** with more hydrophobic molecules, we introduced several amide-coupled pyridines (series **6**). None of these modifications substantially improved the IC_{50} of this series, as their IC_{50} values ranged from 4.04 μM (**6c**) to 8.37 μM (**6a**). Despite their ability to inhibit Mac1 *in vitro*, **6a-6c** were unable to repress virus replication, while **6d** and **6e** were modest inhibitors of MHV replication, and **6e** also inhibited SARS-CoV-2 in the presence of IFN-γ. The reason for this discrepancy is unclear, though it is noted that both **6d** and **6e** have nitrogen atoms in the 2 position of the pyridine ring, while **6a** and **6b** have the nitrogen in the 4 position. Regardless, structural insights from inhibitors such as **4a** and **4b** provide a foundation for developing next-generation inhibitors that can more effectively enter cells and demonstrate robust antiviral activity *in vivo*. Future strategies to optimize the Mac1 inhibitor antiviral activity will include *i)* improving their pharmacokinetic properties, *ii)* developing alternative delivery methods such as using nanoparticles to address the drug-delivery challenges, and *iii)* structural modifications that enhance the compounds' ability to penetrate deeper into the Mac1 binding pocket and increase binding affinity.

To demonstrate the specificity of our hit compounds for Mac1 during infection, we first tested both **5c** and **6e** for inhibition of SARS-CoV-2 in the presence and absence of IFN-γ, as we have done previously (40). Each compound only inhibited virus replication in the presence of IFN-γ, which strongly indicates that these compounds target Mac1, as it is unlikely that there are other viral proteins where inhibition would demonstrate such stark differences between IFN-γ-treated and untreated cells. To further confirm specificity, we passaged MHV in the presence of **5a** with the goal of identifying drug-resistant mutations. We identified a resistant virus, and interestingly, it contained a two-amino-acid mutation in Mac1, A1438T/G1439V, which we observed previously after passaging MHV in the presence of a separate compound (40). Having the same mutation appear after passaging MHV in the presence of two different Mac1 inhibitors indicates that Mac1 is highly constrained in the ADP-ribose binding pocket and has limited options for developing resistance. We also previously reported that MHV A1438T/G1439V is highly attenuated in mice, indicating a fitness trade-off with the development of drug resistance against Mac1 targeting compounds.

In summary, our findings underscore the potential of pyrrolo-pyrimidine-based compounds as both therapeutic agents and molecular probes, enabling more profound insights into the role of Mac1 in CoV biology. By refining these inhibitors through targeted structural modifications and addressing pharmacokinetic limitations, we will continue to enhance their efficacy and therapeutic profiles. As we further investigate the mechanisms of Mac1 and its impact on viral replication, we will enable the development of innovative strategies to mitigate the threat posed by highly pathogenic human coronaviruses and potentially other emerging pathogens.

METHODS

Chemistry. See supplemental methods.

Cell culture and reagents. Delayed brain tumor (DBT), L929, Vero E6, HeLa cells expressing the MHV receptor carcinoembryonic antigen-related cell adhesion molecule 1 (CEACAM1) (HeLa-MHVR), and baby hamster kidney cells expressing CEACAM1 (BHK-MVR) (all cell lines gifts provided by Stanley Perlman, University of Iowa) were grown in Dulbecco's modified Eagle medium (DMEM) supplemented with 10% fetal bovine serum (FBS), 100 U/ml penicillin, 100 mg/ml streptomycin, HEPES, sodium pyruvate, nonessential amino acids, and L-glutamine. Calu-3 cells (ATCC) were grown in MEM supplemented with 20% FBS. Human IFN-γ was purchased from R&D Systems. ADP-ribosylated and control peptides were purchased from Cambridge peptides. Recombinant SARS-CoV-2 proteins was expressed with an N-terminal His-tag from a pET21a+ expression vector and purified as previously described (11).

Crystallization, data collection, processing and refinement. Protein crystallization was performed using sitting-drop vapour-diffusion method in a Swissci 3D 96-well plate. The well solution contained the reported crystallization condition (33) but varied in PEG 3000 concentration: 0.1 M CHES pH 9.5, 28-32% PEG (v/v) 3000. 100 nL of 0.8 mM SARS-CoV-2 Mac1 was mixed with 100 nL of the crystallization solution using Mosquito pipetting robot (TTP Labtech). Crystals grew within 24 hr. Crystals from one droplet were then crushed, diluted in 100 µL reservoir solution and used as seeding solution. 0.8 mM SARS-CoV-2 Mac1 and 5 mM inhibitor were mixed and incubated at RT for 30 min. Crystallization drops were set up by mixing 100 nL of SARS- CoV-2 Mac1 and ligand solution and 100 nL of the reservoir solution. Then streak seeding was performed. Crystallization plates were monitored at RT with IceBear (47) and co-crystals appeared within 24 hr. For cryo-cooling, the crystals were soaked in 0.1 M CHES pH 9.5, 32% PEG

(v/v) 3000 with 0.5 mM of the compound. X-ray diffraction data were collected on beamline BioMAX at MAX IV, Lund, Sweden. The dataset was processed by the XDS program package via XDSGUI (Table S1) (48, 49).

The structures were solved with PHASER (50) by the method of molecular replacement by using SARS-CoV-2 Mac1 (PDB: 8TV6) as a search model. Model building and refinement were performed with Coot (51) and REFMAC5 (52), respectively (Table S1). The structures were visualized in PyMOL version 1.7.2.1 (Schrödinger).

Docking. The solved structure of 4a with Mac1 was prepared using the Schrödinger Protein Preparation Wizard (schrödinger.com), which adds hydrogens, predicts protonation status of titratable groups, optimizes hydrogen bonds, and then performs a constrained minimization. Only the water networks near the ligand were retained. Ligands were prepared using LigPrep and then docked into the receptor using Glide with XP precision (53, 54). The top scoring models were refined using Prime mmGBSA, allowing flexibility of the ligand and any residue/water within 5 Å of the ligand (55, 56).

AlphaScreen (AS) assay. The AlphaScreen reactions were carried out in 384-well plates (Alphaplate, PerkinElmer, Waltham, MA) in a total volume of 40 µL in buffer containing 25 mM HEPES (pH 7.4), 100 mM NaCl, 0.5 mM TCEP, 0.1% BSA, and 0.05% CHAPS. All reagents were prepared as 4× stocks and 10 µL volume of each reagent was added to a final volume of 40 µL. All compounds were transferred acoustically using ECHO 555 (Beckman Inc) and preincubated after mixing with purified His-tagged macrodomain protein (250 nM) for 30 min at RT, followed by addition of a 10 amino acid biotinylated and ADP-ribosylated peptide [ARTK(Bio) QTARK (Aoa-RADP)S] (Cambridge peptides) (625 nM). After 1 h incubation at RT, streptavidin-coated donor beads (7.5 µg/mL) and nickel chelate acceptor beads (7.5 µg/mL); (PerkinElmer AlphaScreen

Histidine Detection Kit) were added under low light conditions, and plates were shaken at 400 rpm for 60 min at RT protected from light. Plates were kept covered and protected from light at all steps and read on BioTek plate reader using an AlphaScreen 680 excitation/570 emission filter set. For counter screening of the compounds, 25 nM biotinylated and hexahistidine-tagged linker peptide (Bn-His6) (PerkinElmer) was added to the compounds, followed by addition of beads as described above. For data analysis, the percent inhibition was normalized to positive (DMSO + labeled peptide) and negative (DMSO + macrodomain + peptide, no ADPr) controls. The IC_{50} values were calculated via four-parametric non-linear regression analysis constraining bottom (=0), top (=100), & Hillslope (=1) for all curves.

Differential scanning fluorimetry (DSF). Thermal shift assay with DSF involved use of LightCycler® 480 Instrument (Roche Diagnostics). In total, a 15 µL mixture containing 8× SYPRO Orange (Invitrogen), and 10 µM macrodomain protein in buffer containing 20 mM HEPES-NaOH, pH 7.5 and various concentrations of ADP-ribose or hit compounds were mixed on ice in 384-well PCR plate (Roche). Fluorescent signals were measured from 25 to 95°C in 0.2 °C/ 30/Sec steps (excitation, 470–505 nm; detection, 540–700 nm). The main measurements were carried out in triplicate. Data evaluation and Tm determination involved use of the Roche LightCycler® 480 Protein Melting Analysis software, and data fitting calculations involved the use of single site binding curve analysis on GraphPad Prism. The thermal shift (ΔT_m) was calculated by subtracting the T_m values of the DMSO from the T_m values of compounds.

Determination of LogD. 0.11 mg of each compound weighed out into 2 mL centrifuge tubes. 1 mL of octanol saturated PBS or 0.1M HCl was added to each centrifuge tube and vortexed to dissolve. Then, 0.5-1.0 mL of the PBS saturated octanol was added to the 0.5-1.0 mL octanol saturated PBS supernatant and vortexed. Next, 100 μl of the octanol saturated PBS phase from

each centrifuge tube was added to separate UPLC vials. 100 μl of 50:50 MP H_2O:ACN was added to each vial and vortexed. The remaining octanol saturated PBS layer was removed from the vial using a micropipette and stored in separate vial. 100 μl of the PBS saturated octanol layer from each centrifuge tube was added to separate UPLC vials. 100 μl of 50:50 MP H_2O:ACN was added to each vial and vortexed. These procedures were repeated in triplicate and then analyzed by UPLC/UV-VIS.

Cell viability assay. Delayed brain tumor (DBT), L929 and Calu3 Cellular metabolic activity was assessed using a CyQUANT MTT cell proliferation assay (Thermo Fisher Scientific) by following the manufacturer's instructions.

Generation of recombinant pBAC-JHM constructs.

Recombinant pBAC-JHMV^{IA} constructs were created using Red recombination as previously described (15). For pBAC-JHMV^{IA}-nLuc, the nano-luciferase gene was amplified with ends homologous to the 5' and 3' end of ORF4 using the following primers:

F 5'-GGCAGCAAGTAGTTATGGCCCTCATCGGTCCCAAGACTACTATTGCTGCT GTCTTCACACTCGAAGATTTCG-3'

R 5'- GGCGTCACTCACAAGCCAAATCTCCATGTAGCTGGTGG TTACGCCAGAATGCGTTCGCACAGCCGCCAGCCGGTCA GCCAGTGTTACAACCAATTAAC-3'

The PCR product was recombined into pBAC-JHMV^{IA} replacing the ORF4 gene, creating pBAC-JHMV^{IA}-nLuc (Fig. S1). pBAC-JHMV^{IA}-A1438T/G1439V was previously described (17). BAC DNA was analyzed by restriction enzyme digest, PCR, and direct sequencing for isolation of correct clones.

Reconstitution of recombinant pBAC-JHMV-derived virus. Approximately 1×10^6 BHK-MVR cells were transfected with approximately 0.5 to 1 µg of pBAC-JHMV^{IA} DNA and 1 µg of pcDNA-MHV-N plasmid using PolyJet (SignaGen) as a transfection reagent. Stocks of the resulting virus were created by infecting ~1.5×10^7 17Cl-1 cells at a multiplicity of infection

(MOI) of 0.1 PFU/cell and collecting both the cells and supernatant at 16 to 20 hpi. The cells were freeze-thawed, and debris was removed prior to collecting virus stocks. Virus stocks were quantified by plaque assay on HeLa-MHVR cells and sequenced with the collection of infected 17Cl-1s or DBT cells using TRIzol. RNA was isolated and cDNA was prepared using MMLV-reverse transcriptase per the manufacturer's instructions (Thermo Fisher Scientific). The nLuc gene sequence was amplified by PCR using the same primers as described above for sequencing BACs, and then resulting PCR products were sequenced by Sanger sequencing. The sequence was analyzed using DNA Star software.

Virus infection. DBT and L929 were infected at an MOI of 0.1 with MHV strains JHMV^{IA}-WT or JHMV^{IA}-nLuc. Calu-3 cells were infected at an MOI of 0.1 with recombinant SARS-CoV-2 (Wuhan strain). For Calu-3 cells, trypsin-TPCK (1 μg/mL) was added to the medium at the time of infection. All infections included a 1-h adsorption phase, except for Calu-3 cells where the adsorption phase was increased to 2 h. Compounds were added after the adsorption phase. Infected cells and supernatants were collected at indicated time points and titers were determined on Hela-MHVR (MHV) or Vero E6 cells (SARS-CoV-2). For IFN-γ pretreatment experiments, human IFN-γ was added to Calu-3 cells 18 to 20 h prior to infection and were maintained in culture media throughout the infection.

Identification of drug resistant MHV mutant viruses. DBT cells were infected in triplicate as described above. After each infection, the viral titer from each individual well was determined and then passaged to a new well of DBT cells. After 3 passages, 2 consecutive plaque picks were performed from 2 of the 3 individually passaged viral samples to collect individual isolates of MHV. RNA was isolated from these isolates using Trizol per manufacturer's instructions. cDNA was prepared using MMLV- reverse transcriptase per the manufacturer's instructions (Thermo

Fisher Scientific) and PCR was performed using the following primers: Forward 5'-ggctgttgtggatggcaagca-3' and Reverse 5'-gctttggtaccagcaacggag-3'. PCR products were sequenced by Sanger Sequencing (Azenta).

Statistical analysis. All statistical analyses were done using a multivariant t-test to assess differences in mean values between groups, and graphs are expressed as geometric means ± geometric standard deviations (SD) (virus titers) or ± standard errors of the means (SEM). All data were analyzed using GraphPad Prism software. Significant *p* values are denoted with asterisks: *, $p \leq 0.05$; **, $p \leq 0.01$; ***, $p \leq 0.001$.

Data availability. Atomic coordinates and structure factors will be available at the Protein Data Bank with the id. 9GUB. Raw diffraction data will be available at fairdata.fi (https://doi.org/10.23729/c2152e19-38ec-4092-878d-f353358cbe5a).

ACKNOWLEDGEMENTS

We thank Stanley Perlman for cell lines, Michael Hageman and the KU BIO Center for performing ADME studies, Mr. Kristopher Mason and Vaccitech for the use of their mass spectrometer, the Oulu Structural Biology core facility, a member of Biocenter Finland, Instruct-ERIC Centre Finland and FINStruct. ARF would like to thank funding from the NIH (R35GM138029), the NIH-funded Chemical Biology of Infectious Diseases (CBID) COBRE at the University of Kansas (P20GM113117), a CTSA grant from NCATS awarded to the University of Kansas for Frontiers: University of Kansas Clinical and Translational Science Institute (#UL1TR002366), a J.R. and Inez Jay Award from the University of Kansas, and a graduate student fellowship from the University of Kansas Madison and Lila Self graduate fellowship (JJP). DF would like to thank funding from the McDaniel College Student-Faculty Summer Research Fund, the Jean Richards Fund, the Schofield fund, and the Scott and Natalie Dahne fund. LL would like to thank funding from the Sidrid Jusélius foundation.

The funders had no role in study design, data collection and analysis, decision to publish, or preparation of the manuscript.

Author contributions:

Conceptualization: JJP, LL, DVF, ARF
Data curation: JJP, MTHD, DC, DKJ, NS, AR, LL, DVF, ARF
Formal analysis: JJP, MTHD, DC, DKJ, AR, LL, DVF, ARF
Funding acquisition: JJP, LL, DVF, ARF
Methodology: JJP, MTHD, DKJ, AR, LL, DVF, ARF
Investigation: JJP, MTHD, DC, LMS, IC, GC, DT, JP, NS, JJOC, PS, DKJ, AR, LL, DVF, ARF
Project administration: LL, DVF, ARF
Resources: DKJ, AR, LL, DVF, ARF
Visualization: JJP, MTHD, DC, LMS, IC, GC, DT, JP, NS, DKJ, AR, LL, DVF, ARF
Validation: JJP, MTHD, DKJ, AR, LL, DVF, ARF
Supervision: DKJ, AR, LL, DVF, ARF
Writing—original draft: JJP, ARF
Writing—review & editing: JJP, MTHD, DC, LMS, IC, GC, DT, JP, NS, JJOC, PS, DKJ, AR, LL, DVF, ARF

A.R.F. was named as an inventor on a patent filed by the University of Kansas for a live-attenuated SARS-CoV-2 vaccine.

REFERENCES

1. Organization WH. 2020. Impact of COVID-19 on people's livelihoods, their health and our food systems. World Health Organization.
2. Zhao J, Wan W, Yu K, Lemey P, Pettersson JH, Bi Y, Lu M, Li X, Chen Z, Zheng M, Yan G, Dai J, Li Y, Haerheng A, He N, Tu C, Suchard MA, Holmes EC, He WT, Su S. 2024. Farmed fur animals harbour viruses with zoonotic spillover potential. Nature 634:228-233.
3. Minkoff JM, tenOever B. 2023. Innate immune evasion strategies of SARS-CoV-2. Nat Rev Microbiol 21:178-194.
4. Yao T, Foo C, Zheng G, Huang R, Li Q, Shen J, Wang Z. 2023. Insight into the mechanisms of coronaviruses evading host innate immunity. Biochim Biophys Acta Mol Basis Dis 1869:166671.
5. Eckei L, Krieg S, Butepage M, Lehmann A, Gross A, Lippok B, Grimm AR, Kummerer BM, Rossetti G, Luscher B, Verheugd P. 2017. The conserved macrodomains of the non-structural proteins of Chikungunya virus and other pathogenic positive strand RNA viruses function as mono-ADP-ribosylhydrolases. Sci Rep 7:41746.
6. Grunewald ME, Chen Y, Kuny C, Maejima T, Lease R, Ferraris D, Aikawa M, Sullivan CS, Perlman S, Fehr AR. 2019. The coronavirus macrodomain is required to prevent PARP-mediated inhibition of virus replication and enhancement of IFN expression. PLoS Pathog 15:e1007756.
7. Luscher B, Ahel I, Altmeyer M, Ashworth A, Bai P, Chang P, Cohen M, Corda D, Dantzer F, Daugherty MD, Dawson TM, Dawson VL, Deindl S, Fehr AR, Feijs KLH, Filippov DV, Gagne JP, Grimaldi G, Guettler S, Hoch NC, Hottiger MO, Korn P, Kraus WL, Ladurner A, Lehtio L, Leung AKL, Lord CJ, Mangerich A, Matic I, Matthews J, Moldovan GL, Moss J, Natoli G, Nielsen ML, Niepel M, Nolte F, Pascal J, Paschal BM, Pawlowski K, Poirier GG, Smith S, Timinszky G, Wang ZQ, Yelamos J, Yu X, Zaja R, Ziegler M. 2022. ADP-ribosyltransferases, an update on function and nomenclature. FEBS J 289:7399-7410.
8. Rack JG, Perina D, Ahel I. 2016. Macrodomains: Structure, Function, Evolution, and Catalytic Activities. Annu Rev Biochem 85:431-54.
9. Fehr AR, Jankevicius G, Ahel I, Perlman S. 2018. Viral Macrodomains: Unique Mediators of Viral Replication and Pathogenesis. Trends Microbiol 26:598-610.
10. Leung AKL, McPherson RL, Griffin DE. 2018. Macrodomain ADP-ribosylhydrolase and the pathogenesis of infectious diseases. PLoS Pathog 14:e1006864.
11. Alhammad YMO, Kashipathy MM, Roy A, Gagne JP, McDonald P, Gao P, Nonfoux L, Battaile KP, Johnson DK, Holmstrom ED, Poirier GG, Lovell S, Fehr AR. 2021. The SARS-CoV-2 Conserved Macrodomain Is a Mono-ADP-Ribosylhydrolase. J Virol 95(3):e01969-20.
12. Putics A, Filipowicz W, Hall J, Gorbalenya AE, Ziebuhr J. 2005. ADP-ribose-1"-monophosphatase: a conserved coronavirus enzyme that is dispensable for viral replication in tissue culture. J Virol 79:12721-31.
13. Eriksson KK, Cervantes-Barragán L, Ludewig B, Thiel V. 2008. Mouse Hepatitis Virus Liver Pathology Is Dependent on ADP-Ribose-1″-Phosphatase, a Viral Function Conserved in the Alpha-Like Supergroup. Journal of Virology 82:12325-12334.
14. Kuri T, Eriksson KK, Putics A, Zust R, Snijder EJ, Davidson AD, Siddell SG, Thiel V, Ziebuhr J, Weber F. 2011. The ADP-ribose-1"-monophosphatase domains of severe acute

563 respiratory syndrome coronavirus and human coronavirus 229E mediate resistance to
564 antiviral interferon responses. J Gen Virol 92:1899-1905.
565 15. Fehr AR, Athmer J, Channappanavar R, Phillips JM, Meyerholz DK, Perlman S. 2015.
566 The nsp3 macrodomain promotes virulence in mice with coronavirus-induced
567 encephalitis. J Virol 89:1523-36.
568 16. Fehr AR, Channappanavar R, Jankevicius G, Fett C, Zhao J, Athmer J, Meyerholz DK,
569 Ahel I, Perlman S. 2016. The Conserved Coronavirus Macrodomain Promotes Virulence
570 and Suppresses the Innate Immune Response during Severe Acute Respiratory Syndrome
571 Coronavirus Infection. mBio 7:10.1128/mbio.01721-16.
572 17. Voth LS, O'Connor JJ, Kerr CM, Doerger E, Schwarting N, Sperstad P, Johnson DK, Fehr
573 AR. 2021. Unique Mutations in the Murine Hepatitis Virus Macrodomain Differentially
574 Attenuate Virus Replication, Indicating Multiple Roles for the Macrodomain in
575 Coronavirus Replication. J Virol 95:e0076621.
576 18. Alhammad YM, Parthasarathy S, Ghimire R, Kerr CM, O'Connor JJ, Pfannenstiel JJ,
577 Chanda D, Miller CA, Baumlin N, Salathe M, Unckless RL, Zuñiga S, Enjuanes L, More
578 S, Channappanavar R, Fehr AR. 2023. SARS-CoV-2 Mac1 is required for IFN
579 antagonism and efficient virus replication in cell culture and in mice. Proceedings of the
580 National Academy of Sciences 120:e2302083120.
581 19. Taha TY, Suryawanshi RK, Chen IP, Correy GJ, McCavitt-Malvido M, O'Leary PC,
582 Jogalekar MP, Diolaiti ME, Kimmerly GR, Tsou CL, Gascon R, Montano M, Martinez-
583 Sobrido L, Krogan NJ, Ashworth A, Fraser JS, Ott M. 2023. A single inactivating amino
584 acid change in the SARS-CoV-2 NSP3 Mac1 domain attenuates viral replication in vivo.
585 PLoS Pathog 19:e1011614.
586 20. Kerr CM, Pfannenstiel JJ, Alhammad YM, Roy A, O'Connor JJ, Ghimire R, Khattabi R,
587 Shrestha R, McDonald PR, Gao P, Johnson DK, More S, Channappanavar R, Fehr AR.
588 2024. Mutation of highly conserved residues in loop 2 of the coronavirus macrodomain
589 demonstrates that enhanced ADP-ribose binding is detrimental to infection. bioRxiv
590 doi:10.1101/2024.01.03.574082.
591 21. McPherson RL, Abraham R, Sreekumar E, Ong SE, Cheng SJ, Baxter VK, Kistemaker
592 HA, Filippov DV, Griffin DE, Leung AK. 2017. ADP-ribosylhydrolase activity of
593 Chikungunya virus macrodomain is critical for virus replication and virulence. Proc Natl
594 Acad Sci U S A 114:1666-1671.
595 22. Abraham R, Hauer D, McPherson RL, Utt A, Kirby IT, Cohen MS, Merits A, Leung
596 AKL, Griffin DE. 2018. ADP-ribosyl-binding and hydrolase activities of the alphavirus
597 nsP3 macrodomain are critical for initiation of virus replication. Proc Natl Acad Sci U S
598 A 115:E10457-E10466.
599 23. Abraham R, McPherson RL, Dasovich M, Badiee M, Leung AKL, Griffin DE. 2020.
600 Both ADP-Ribosyl-Binding and Hydrolase Activities of the Alphavirus nsP3
601 Macrodomain Affect Neurovirulence in Mice. mBio 11;11(3):e01969-20
602 24. Saikatendu KS, Joseph JS, Subramanian V, Clayton T, Griffith M, Moy K, Velasquez J,
603 Neuman BW, Buchmeier MJ, Stevens RC, Kuhn P. 2005. Structural basis of severe acute
604 respiratory syndrome coronavirus ADP-ribose-1"-phosphate dephosphorylation by a
605 conserved domain of nsP3. Structure 13:1665-75.
606 25. Egloff MP, Malet H, Putics A, Heinonen M, Dutartre H, Frangeul A, Gruez A,
607 Campanacci V, Cambillau C, Ziebuhr J, Ahola T, Canard B. 2006. Structural and

functional basis for ADP-ribose and poly(ADP-ribose) binding by viral macro domains. J Virol 80:8493-502.

26. Xu Y, Cong L, Chen C, Wei L, Zhao Q, Xu X, Ma Y, Bartlam M, Rao Z. 2009. Crystal structures of two coronavirus ADP-ribose-1"-monophosphatases and their complexes with ADP-Ribose: a systematic structural analysis of the viral ADRP domain. J Virol 83:1083-92.

27. Malet H, Coutard B, Jamal S, Dutartre H, Papageorgiou N, Neuvonen M, Ahola T, Forrester N, Gould EA, Lafitte D, Ferron F, Lescar J, Gorbalenya AE, de Lamballerie X, Canard B. 2009. The crystal structures of Chikungunya and Venezuelan equine encephalitis virus nsP3 macro domains define a conserved adenosine binding pocket. J Virol 83:6534-45.

28. Hammond RG, Schormann N, McPherson RL, Leung AKL, Deivanayagam CCS, Johnson MA. 2021. ADP-ribose and analogues bound to the deMARylating macrodomain from the bat coronavirus HKU4. Proc Natl Acad Sci U S A 118. 2;118(2):e2004500118

29. Cho CC, Lin MH, Chuang CY, Hsu CH. 2016. Macro Domain from Middle East Respiratory Syndrome Coronavirus (MERS-CoV) Is an Efficient ADP-ribose Binding Module: CRYSTAL STRUCTURE AND BIOCHEMICAL STUDIES. J Biol Chem 291:4894-902.

30. Allen MD, Buckle AM, Cordell SC, Lowe J, Bycroft M. 2003. The crystal structure of AF1521 a protein from Archaeoglobus fulgidus with homology to the non-histone domain of macroH2A. J Mol Biol 330:503-11.

31. Frick DN, Virdi RS, Vuksanovic N, Dahal N, Silvaggi NR. 2020. Molecular Basis for ADP-Ribose Binding to the Mac1 Domain of SARS-CoV-2 nsp3. Biochemistry 59:2608-2615.

32. Lin MH, Chang SC, Chiu YC, Jiang BC, Wu TH, Hsu CH. 2020. Structural, Biophysical, and Biochemical Elucidation of the SARS-CoV-2 Nonstructural Protein 3 Macro Domain. ACS Infect Dis 6:2970-2978.

33. Michalska K, Kim Y, Jedrzejczak R, Maltseva NI, Stols L, Endres M, Joachimiak A. 2020. Crystal structures of SARS-CoV-2 ADP-ribose phosphatase: from the apo form to ligand complexes. IUCrJ 7:814-824.

34. Rack JGM, Zorzini V, Zhu Z, Schuller M, Ahel D, Ahel I. 2020. Viral macrodomains: a structural and evolutionary assessment of the pharmacological potential. Open Biol 10:200237.

35. Schuller M, Correy GJ, Gahbauer S, Fearon D, Wu T, Diaz RE, Young ID, Carvalho Martins L, Smith DH, Schulze-Gahmen U, Owens TW, Deshpande I, Merz GE, Thwin AC, Biel JT, Peters JK, Moritz M, Herrera N, Kratochvil HT, Consortium QSB, Aimon A, Bennett JM, Brandao Neto J, Cohen AE, Dias A, Douangamath A, Dunnett L, Fedorov O, Ferla MP, Fuchs MR, Gorrie-Stone TJ, Holton JM, Johnson MG, Krojer T, Meigs G, Powell AJ, Rack JGM, Rangel VL, Russi S, Skyner RE, Smith CA, Soares AS, Wierman JL, Zhu K, O'Brien P, Jura N, Ashworth A, Irwin JJ, Thompson MC, Gestwicki JE, et al. 2021. Fragment binding to the Nsp3 macrodomain of SARS-CoV-2 identified through crystallographic screening and computational docking. Sci Adv 14;7(16):eabf8711.

36. Schuller M, Zarganes-Tzitzikas T, Bennett J, De Cesco S, Fearon D, von Delft F, Fedorov O, Brennan PE, Ahel I. 2023. Discovery and Development Strategies for SARS-CoV-2 NSP3 Macrodomain Inhibitors. Pathogens 15;12(2):324.

37. Gahbauer S, Correy GJ, Schuller M, Ferla MP, Doruk YU, Rachman M, Wu T, Diolaiti M, Wang S, Neitz RJ, Fearon D, Radchenko DS, Moroz YS, Irwin JJ, Renslo AR, Taylor JC, Gestwicki JE, von Delft F, Ashworth A, Ahel I, Shoichet BK, Fraser JS. 2023. Iterative computational design and crystallographic screening identifies potent inhibitors targeting the Nsp3 macrodomain of SARS-CoV-2. Proc Natl Acad Sci U S A 120:e2212931120.
38. Roy A, Alhammad YM, McDonald P, Johnson DK, Zhuo J, Wazir S, Ferraris D, Lehtio L, Leung AKL, Fehr AR. 2022. Discovery of compounds that inhibit SARS-CoV-2 Mac1-ADP-ribose binding by high-throughput screening. Antiviral Res 203:105344.
39. Sherrill LM, Joya EE, Walker A, Roy A, Alhammad YM, Atobatele M, Wazir S, Abbas G, Keane P, Zhuo J, Leung AKL, Johnson DK, Lehtio L, Fehr AR, Ferraris D. 2022. Design, synthesis and evaluation of inhibitors of the SARS-CoV-2 nsp3 macrodomain. Bioorg Med Chem 67:116788.
40. Wazir S, Parviainen TAO, Pfannenstiel JJ, Duong MTH, Cluff D, Sowa ST, Galera-Prat A, Ferraris D, Maksimainen MM, Fehr AR, Heiskanen JP, Lehtio L. 2024. Discovery of 2-Amide-3-methylester Thiophenes that Target SARS-CoV-2 Mac1 and Repress Coronavirus Replication, Validating Mac1 as an Antiviral Target. J Med Chem 67:6519-6536.
41. Brosey CA, Houl JH, Katsonis P, Balapiti-Modarage LPF, Bommagani S, Arvai A, Moiani D, Bacolla A, Link T, Warden LS, Lichtarge O, Jones DE, Ahmed Z, Tainer JA. 2021. Targeting SARS-CoV-2 Nsp3 macrodomain structure with insights from human poly(ADP-ribose) glycohydrolase (PARG) structures with inhibitors. Prog Biophys Mol Biol 163:171-186.
42. Tsika AC, Fourkiotis NK, Charalampous P, Gallo A, Spyroulias GA. 2022. NMR study of macro domains (MDs) from betacoronavirus: backbone resonance assignments of SARS-CoV and MERS-CoV MDs in the free and the ADPr-bound state. Biomol NMR Assign 16:9-16.
43. Correy GJ, Kneller DW, Phillips G, Pant S, Russi S, Cohen AE, Meigs G, Holton JM, Gahbauer S, Thompson MC, Ashworth A, Coates L, Kovalevsky A, Meilleur F, Fraser JS. 2022. The mechanisms of catalysis and ligand binding for the SARS-CoV-2 NSP3 macrodomain from neutron and x-ray diffraction at room temperature. Sci Adv 8:eabo5083.
44. Dasovich M, Zhuo J, Goodman JA, Thomas A, McPherson RL, Jayabalan AK, Busa VF, Cheng SJ, Murphy BA, Redinger KR, Alhammad YMO, Fehr AR, Tsukamoto T, Slusher BS, Bosch J, Wei H, Leung AKL. 2022. High-Throughput Activity Assay for Screening Inhibitors of the SARS-CoV-2 Mac1 Macrodomain. ACS Chem Biol 17:17-23.
45. O'Connor JJ, Ferraris D, Fehr AR. 2023. An Update on the Current State of SARS-CoV-2 Mac1 Inhibitors. Pathogens 7;12(10):1221.
46. Ontiveros E, Kuo L, Masters PS, Perlman S. 2001. Inactivation of expression of gene 4 of mouse hepatitis virus strain JHM does not affect virulence in the murine CNS. Virology 289:230-8.
47. Daniel E, Maksimainen MM, Smith N, Ratas V, Biterova E, Murthy SN, Rahman MT, Kiema TR, Sridhar S, Cordara G, Dalwani S, Venkatesan R, Prilusky J, Dym O, Lehtio L, Koski MK, Ashton AW, Sussman JL, Wierenga RK. 2021. IceBear: an intuitive and versatile web application for research-data tracking from crystallization experiment to PDB deposition. Acta Crystallogr D Struct Biol 77:151-163.

48. Brehm W, Trivino J, Krahn JM, Uson I, Diederichs K. 2023. XDSGUI: a graphical user interface for XDS, SHELX and ARCIMBOLDO. J Appl Crystallogr 56:1585-1594.
49. Kabsch W. 2010. Xds. Acta Crystallogr D Biol Crystallogr 66:125-32.
50. McCoy AJ, Grosse-Kunstleve RW, Adams PD, Winn MD, Storoni LC, Read RJ. 2007. Phaser crystallographic software. J Appl Crystallogr 40:658-674.
51. Emsley P, Lohkamp B, Scott WG, Cowtan K. 2010. Features and development of Coot. Acta Crystallogr D Biol Crystallogr 66:486-501.
52. Murshudov GN, Skubak P, Lebedev AA, Pannu NS, Steiner RA, Nicholls RA, Winn MD, Long F, Vagin AA. 2011. REFMAC5 for the refinement of macromolecular crystal structures. Acta Crystallogr D Biol Crystallogr 67:355-67.
53. Friesner RA, Banks JL, Murphy RB, Halgren TA, Klicic JJ, Mainz DT, Repasky MP, Knoll EH, Shelley M, Perry JK, Shaw DE, Francis P, Shenkin PS. 2004. Glide: a new approach for rapid, accurate docking and scoring. 1. Method and assessment of docking accuracy. J Med Chem 47:1739-49.
54. Friesner RA, Murphy RB, Repasky MP, Frye LL, Greenwood JR, Halgren TA, Sanschagrin PC, Mainz DT. 2006. Extra precision glide: docking and scoring incorporating a model of hydrophobic enclosure for protein-ligand complexes. J Med Chem 49:6177-96.
55. Jacobson MP, Friesner RA, Xiang Z, Honig B. 2002. On the role of the crystal environment in determining protein side-chain conformations. J Mol Biol 320:597-608.
56. Jacobson MP, Pincus DL, Rapp CS, Day TJ, Honig B, Shaw DE, Friesner RA. 2004. A hierarchical approach to all-atom protein loop prediction. Proteins 55:351-67.

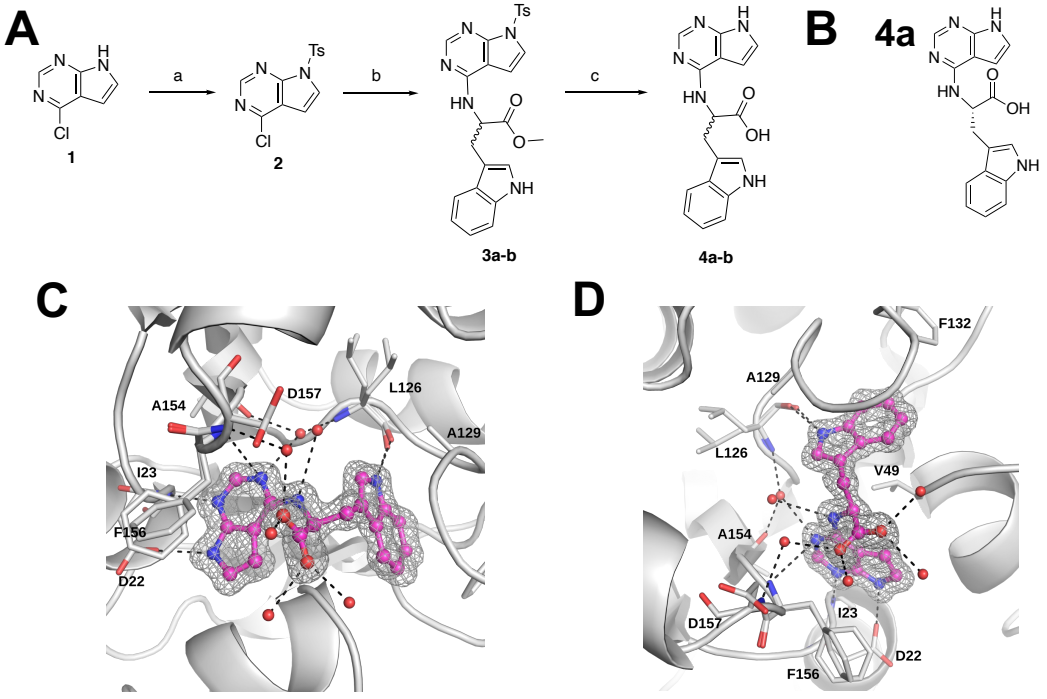

Fig 1. Crystal structure of 4a provides new insight into its interaction with Mac1. (A-B) Chemical synthesis plan to produce **4a-b** (A), and the chemical structure of **4a** (B). (C-D) Crystal structure of **4a** in two different poses (PDB id. 9GUB). These poses include images where the pyrrolo-pyrimidine is oriented in the front left (C) or in the lower middle (D). Note that the carboxylate makes hydrogen bonds with 3 different water molecules and the tryptophanate makes a hydrogen bond with the backbone of L126. The sigma-A weighted 2Fo-Fc electron density map is contoured at 1.0 σ. Waters are shown as red spheres, and hydrogen bonds are illustrated as black dashed lines.

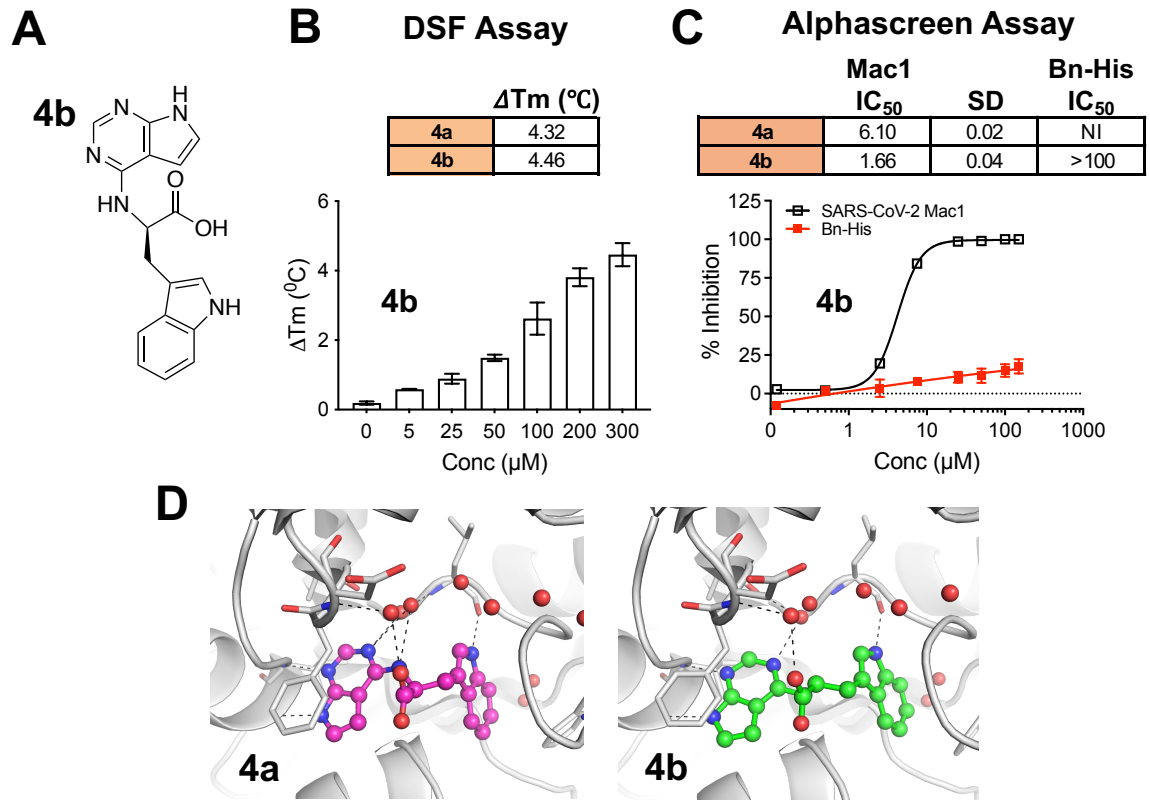

Fig 2. Compound 4b interacts with Mac1 and inhibits Mac1-ADP-ribose binding. A) Chemical structure of compound **4b**. B) Compound **4b** was incubated with SARS-CoV-2 Mac1 at increasing concentrations and the thermal stability of SARS-CoV-2 Mac1 was determined by a DSF assay. The *Δ*Tm is the average 5 experimental replicates. n=5. C) Competition assays were used to demonstrate that **4a** and **4b** block the interaction between Mac1 and ADP-ribosylated peptides in the AS assay. The IC_{50} represents the average value of 2 independent experiments, each done with 3 experimental replicates. The graphs are from one experiment representative of 2 independent experiments. D) Compounds **4a** and **4b** were docked into Mac1 using PDB: 9GUB. Hydrogen bonds are illustrated as dashed lines.

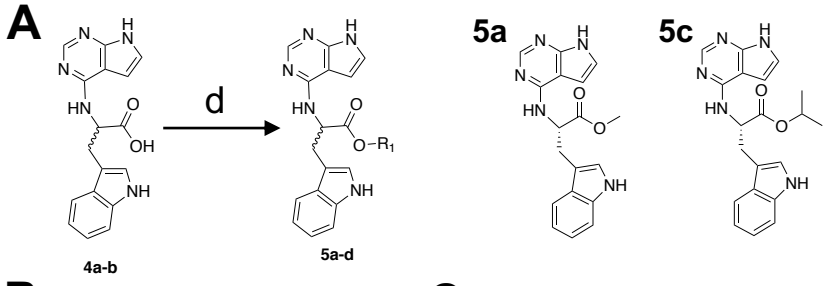

Fig 3. Compounds 5a and 5c interact with Mac1 and inhibit Mac1-ADP-ribose binding. A) Modification of **4a-b** to ester derivatives **5a** and **5c**. B) Compounds **5a** and **5c** were incubated with SARS-CoV-2 Mac1 at increasing concentrations and the thermal stability of SARS-CoV-2 Mac1 was determined by a DSF assay. The *Δ*Tm is the average 5 experimental replicates. n=5. C) Competition assays were used to demonstrate that **5a** and **5c** block the interaction between Mac1 and ADP-ribosylated peptides in the AS assay. The IC_{50} represents the average value of 2 independent experiments. n=3 experimental replicates. D) Compounds **5a** and **5c** were docked into Mac1 using PDB: 9GUB. Hydrogen bonds are illustrated as dashed lines. E) The LogD values were experimentally determined using the shake-flask method for **4a**, **5a**, and **5c**.

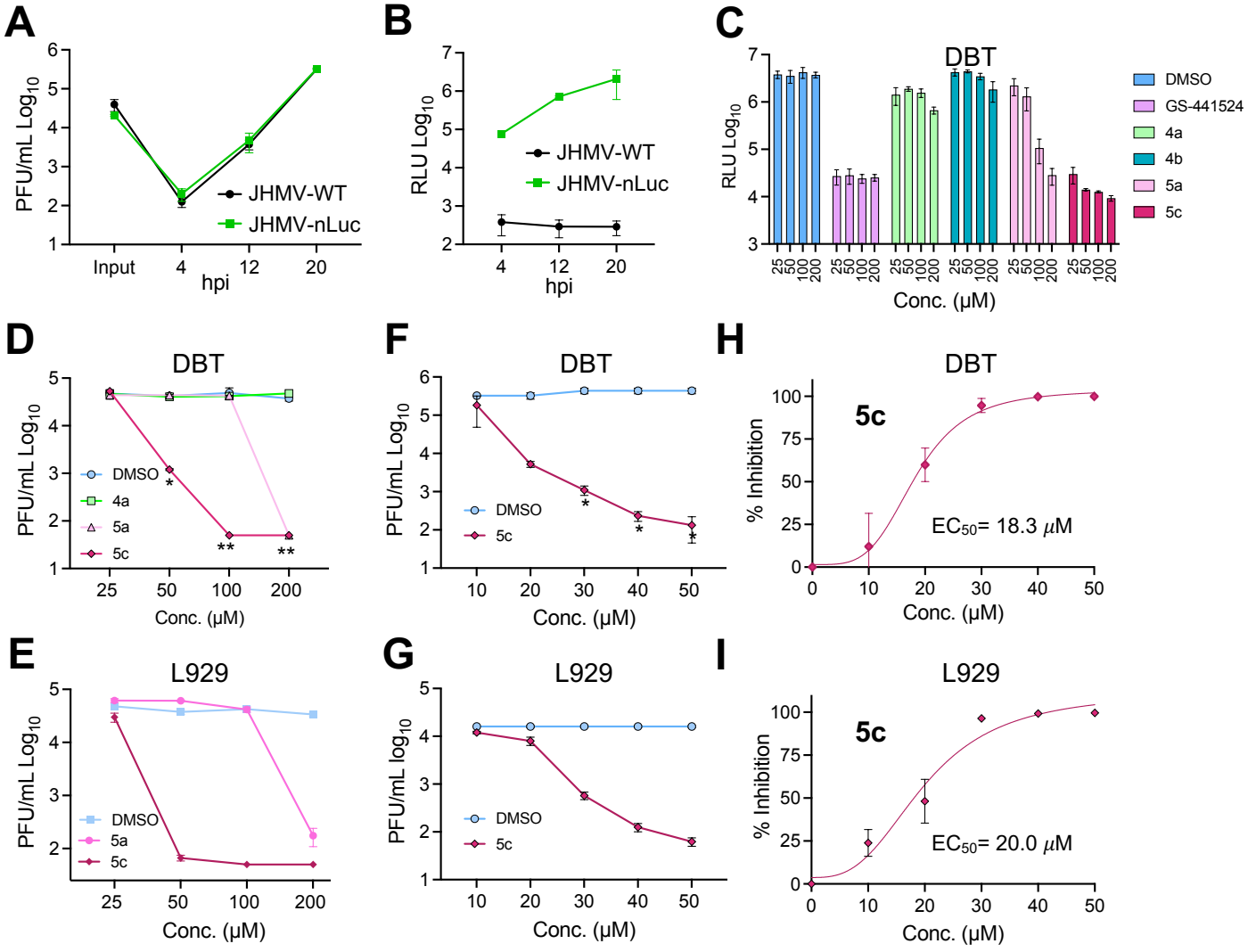

Fig 4. Compounds 5a and 5c, but not 4a, inhibit MHV replication. A) 17Cl-1 cells were infected with JHMV-WT and JHMV-nLuc viruses at an MOI = 0.1. Cells and supernatants were collected at indicated timepoints and progeny virus was determined by plaque assay. B) 17Cl-1 cells were infected as described in A. Lysates were collected at indicated times and luciferase activity was determined using a nano-Glo luciferase assay kit measured as per manufacturer's instructions. The results in A and B are from 1 experiment representative of 2 independent experiments. N=3 biological replicates. C) DBT cells were infected with JHMV-nLuc at an MOI = 0.1 and at 1 hpi, the indicated concentration of each compound was added to the media. Lysates were collected at 20 hpi and luciferase activity was measured as described in B. D-E) DBT cells were infected with JHMV-WT and at 1 hpi the indicated concentration of each compound was added to the media. Cells and supernatants were collected at 20 hpi and progeny virus was measured by plaque assay. The results in C-E are from 1 experiment representative of 2 independent experiments. n=3 biological replicates. F) The combined average % JHMV-WT inhibition of 10-50 μM **5c** on DBT cells over 2 independent experiments. G-H) L929 cells were infected with JHMV-WT and at 1 hpi the indicated concentration of each compound was added to the media. Cells and supernatants were collected at 20 hpi and progeny virus was measured by plaque assay. The results in G-H are from 1 experiment representative of 2 independent experiments. n=3. I) The combined average % JHMV-WT inhibition of 10-50 μM **5c** on DBT cells over 3 independent experiments. The results in C, D, E, G, and H are from 1 experiment representative of 3 independent experiments. N=3 biological replicates.

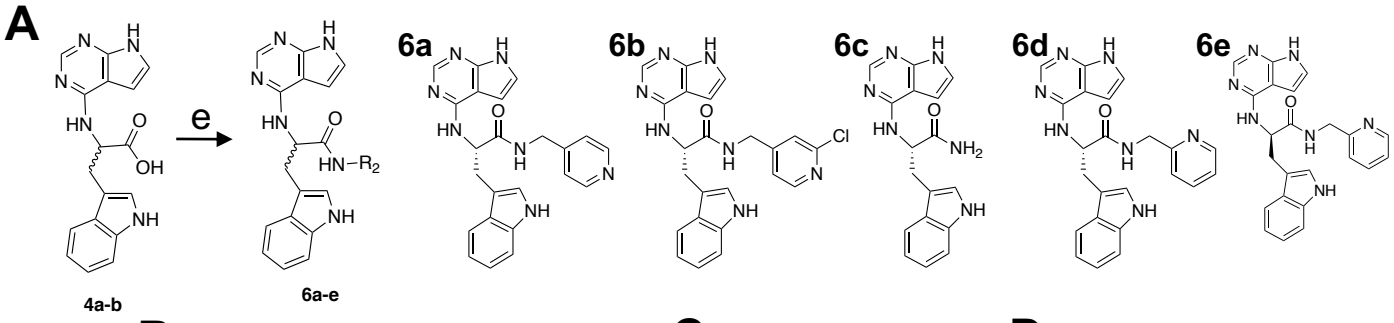

B

Alphascreen Assay

	Mac1 IC_{50}	SD	Bn-His IC_{50}
6a	8.37	0.84	>100
6b	7.57	1.52	>100
6c	4.04	0.27	>100
6d	7.58	1.91	79.24
6e	4.85	0.72	39.65

C

DSF Assay

	ΔTm (℃)
6a	1.29
6b	1.57
6c	3.06
6d	1.39
6e	1.17

D

cLogD

	pH 7.4
6a	1.89
6b	2.72
6c	1.16
6d	1.97
6e	1.97

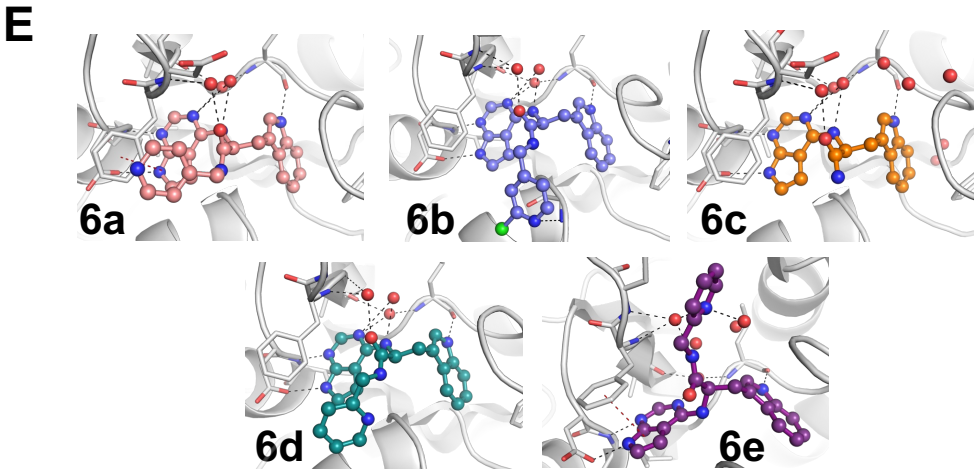

Fig 5. Group 6 compounds interact with Mac1 and inhibit Mac1-ADP-ribose binding. A) Modification of **4a-b** to several new derivatives, **6a-6e. 6a-6d** are derivatives of **4a** while **6e** is a derivates of **4b**. B) Competition assays were used to demonstrate that **6a-6e** block the interaction between Mac1 and ADP-ribosylated peptides in the AS assay. C) Compounds **6a-6e** were incubated with SARS-CoV-2 Mac1 at increasing concentrations and the thermal stability of SARS-CoV-2 Mac1 was determined by a DSF assay. Quantification data in B-C represents the average value of 2 independent experiments. D) Predicted cLogD values of **6a-6e**. E) Compounds **6a-6e** were docked into Mac1. Hydrogen bonds are illustrated as dashed lines.

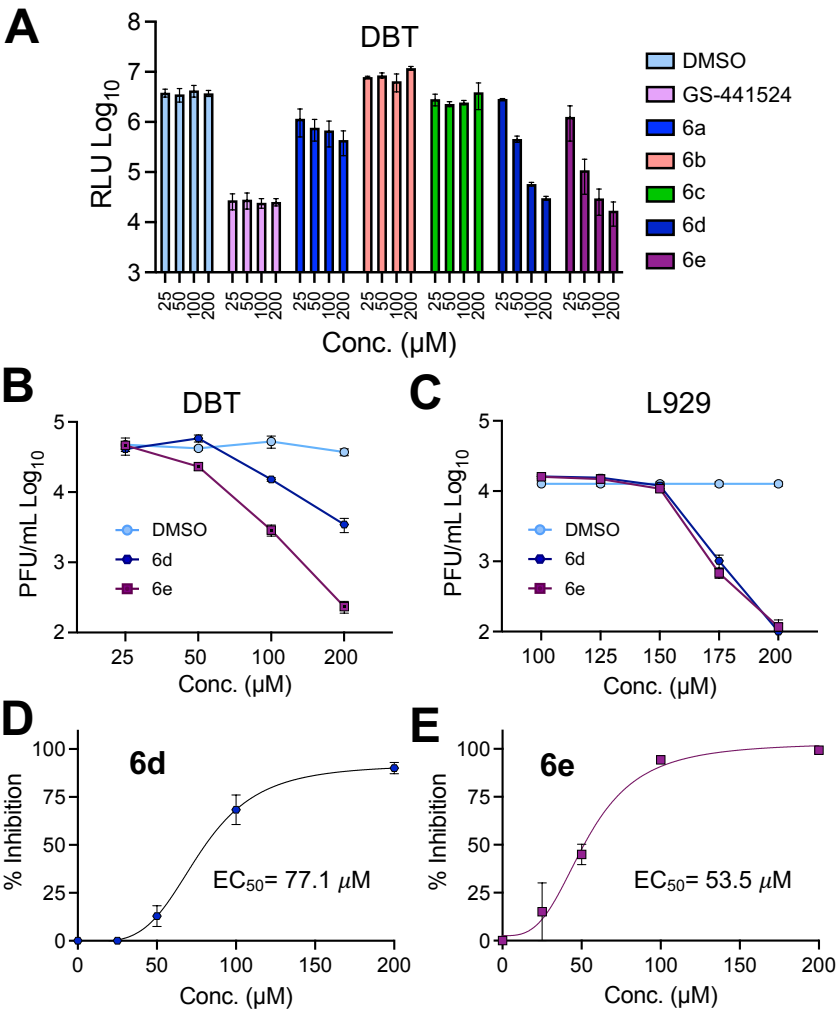

Fig 6. Group 6 compounds interact with Mac1 and inhibit Mac1-ADP-ribose binding. A) Modification of **4a-b** to several new derivatives, **6a-6e. 6a-6d** are derivatives of **4a** while **6e** is a derivates of **4b**. B) Competition assays were used to demonstrate that **6a-6e** block the interaction between Mac1 and ADP-ribosylated peptides in the AS assay. C) Compounds **6a-6e** were incubated with SARS-CoV-2 Mac1 at increasing concentrations and the thermal stability of SARS-CoV-2 Mac1 was determined by a DSF assay. The IC_{50} and ΔTm values in B-C represent the average value of 2 independent experiments, each done with 3 experimental replicates. D) Predicted cLogD values of **6a-6e**. E) Compounds **6a-6e** were docked into Mac1 using PDB: 9GUB. Hydrogen bonds are illustrated as dashed lines.

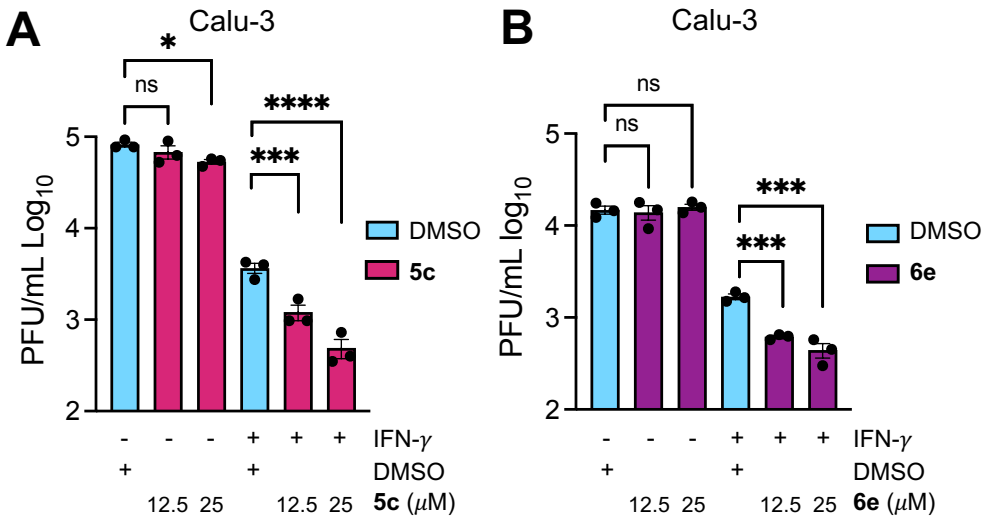

Fig 7. Compounds 5c and 6e inhibit SARS-CoV-2 replication. A-B) Calu-3 cells were mock or IFN-γ pre-treated (100 U) for 18 h, then were infected with SARS-CoV-2 and at 1 hpi the indicated concentration of **5c** (A) or **6e** (B) was added to the media. Cells and supernatants were collected at 20 hpi and progeny virus was measured by plaque assay. The results in A-B are from one experiment representative of 3 independent experiments. N=3 biological replicates.

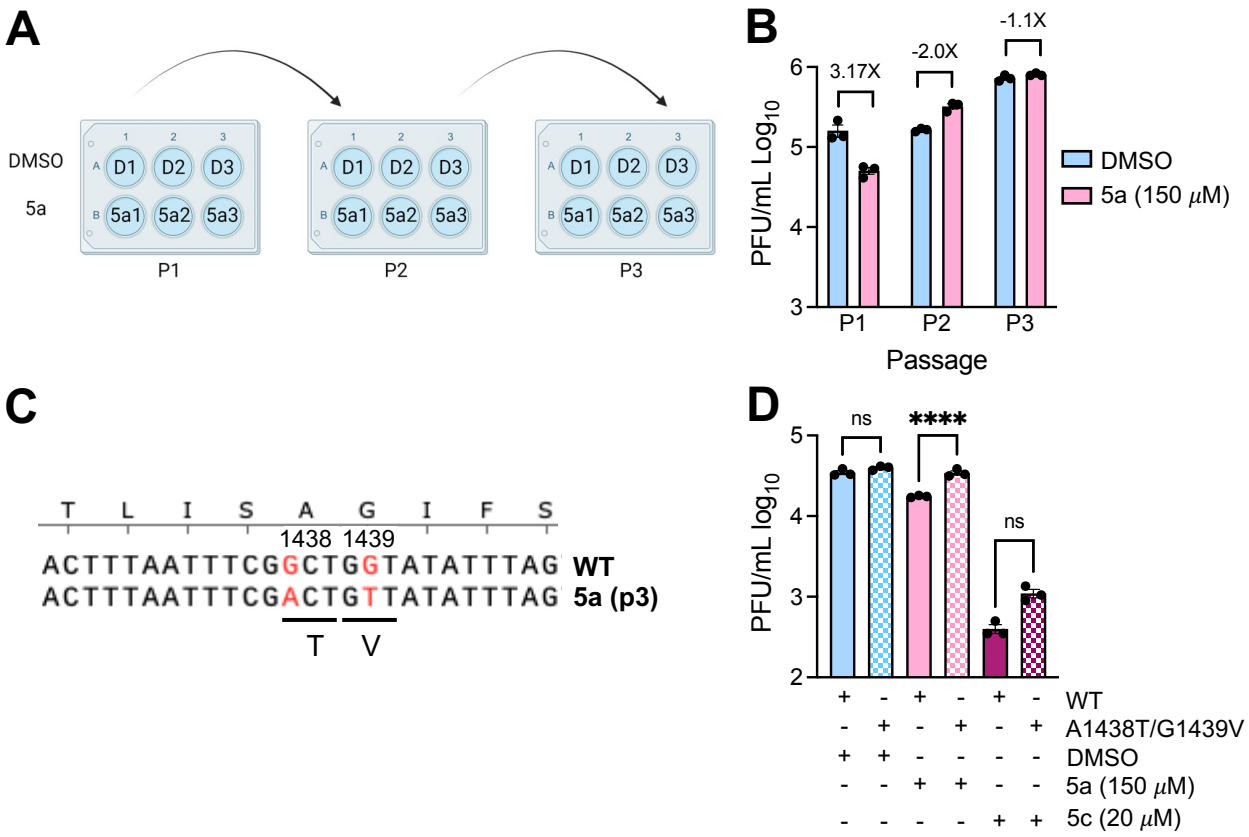

Fig 8. Identification of a Mac1 drug-resistant mutation. A) Cartoon depiction of passaging method for creating drug-resistant virus. 3 separate wells of DBT cells were initially infected with 0.1 MOI MHV in the presence of DMSO or **5a**. Each well was then passaged by taking 100 µl of cells/supernatants from the prior passage and infected a new well of DBT cells. Image was created using BioRender.com. B) Cells and supernatants were collected at 18-20 hpi at each passage and progeny virus was measured by plaque assay. C) Progeny virus at passage 3 was sequenced, which identified a two amino acid A1439T/G1439V mutation. D) DBT cells were infected with WT or A1438T/G1439V recombinant virus at an MOI of 0.1 in the presence of DMSO, **5a**, or **5c**. Cells and supernatants were collected at 20 hpi and progeny virus was measured by plaque assay. The data in D is from 1 experiment representative of 3 independent experiments. N=3 biological replicates.